A Generalized Method for Analyzing Shielded Thin Microstrip Discontinuities

LAWRENCE P. DUNLEAVY AND PISTI B. KATEHI, MEMBER, IEEE

Abstract—**A new integral equation method is described for the accurate full-wave analysis of shielded thin microstrip discontinuities. The integral equation is derived by applying the reciprocity theorem, then solved by the method of moments. In this derivation, a coaxial aperture is modeled with an equivalent magnetic current and is used as the excitation mechanism for generating the microstrip currents. Computational aspects of the method have been explored extensively. A summary of some of the more interesting conclusions is included.**

I. INTRODUCTION

THE NEED FOR more accurate microstrip circuit simulations has become increasingly apparent with the advent of monolithic microwave integrated circuits (MMIC's), as well as the increased interest in millimeter-wave and near-millimeter-wave frequencies. The development of more accurate microstrip discontinuity models, based on full-wave analyses, is of the utmost importance in improving high-frequency circuit simulations and reducing lengthy design cycle costs. Further, in most applications the microstrip circuit is enclosed in a shielding cavity (or housing) as shown in Fig. 1. There are two main conditions where shielding effects are significant: 1) when the frequency approaches or is above the cutoff frequency f_c for higher order modes and 2) when the metal enclosure is physically close to the circuitry. A full-wave analysis is required to accurately model these effects.

Although shielding effects have been studied to some extent in the past (e.g. [1]), the treatment has been incomplete, particularly for more complicated structures such as coupled line filters. Further, shielding effects are not accurately accounted for in the discontinuity models of most available microwave CAD software. To address these inadequacies, this paper develops an accurate method for analyzing thin strip discontinuities in shielded microstrip. The method presented is based on an integral equation approach. The integral equation is derived by an application of the reciprocity theorem and is then solved by the method of moments.

Manuscript received April 19, 1988; revised August 29, 1988. This work was supported primarily by the National Science Foundation under Contract ECS-8602530. Support was also provided by the Army Research Office under Contract DAAL03-87-K-0088 and by the Microwave Products Division of Hughes Aircraft Company.

L. P. Dunleavy was with the Department of Electrical Engineering and Computer Science, University of Michigan, Ann Arbor, MI. He is now with the Industrial Electronics Group, Hughes Aircraft Company, Torrance, CA.

P. B. Katehi is with the Department of Electrical Engineering and Computer Science, University of Michigan, Ann Arbor, MI 48109-2122.

IEEE Log Number 8824528.

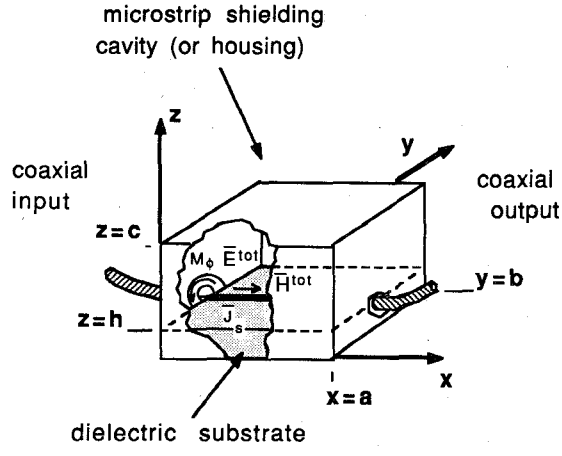

Fig. 1. Basic shielded microstrip geometry.

To derive a realistically based formulation, a coaxial excitation mechanism is used. To date, all full-wave analyses of microstrip discontinuities use either a gap generator excitation method [2]–[4] or a cavity resonance technique [5], [6]. Both of these techniques are purely mathematical tools. The former has no physical basis relative to an actual circuit. The latter is also abstract, since in any practical circuit some form of excitation is present. In fact, one of the most common excitations in practice comes from a coaxial feed (Fig. 1). A magnetic current model for such a feed is used in the present treatment as the excitation.

In addition to developing the theory, computational aspects of the solution are explored extensively. This is an important area that has been largely neglected in the presentation of numerical solutions of this nature. Most significantly, it is shown that an optimum sampling range may be specified that dictates how to divide the conducting strip for best computational accuracy. The method developed in this paper has been applied to study the effect of shielding on the characteristics of discontinuities of the type shown in Fig. 2. Numerical results from this study are presented in a companion paper [7] and are seen to be in excellent agreement with measured data.

II. THEORETICAL FORMULATION

The details of the theoretical derivation for the present method are given in [8]. Hence, only a summary of the key steps is described below.

0018-9480/88/1200-1758$01.00

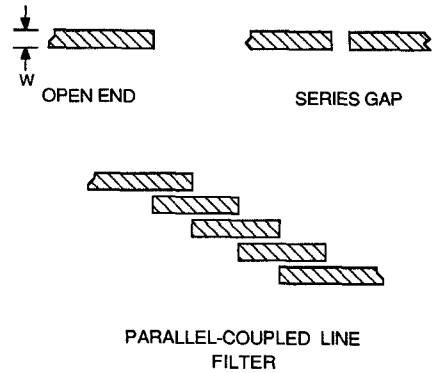

Fig. 2. Discontinuity structures addressed in the present research.

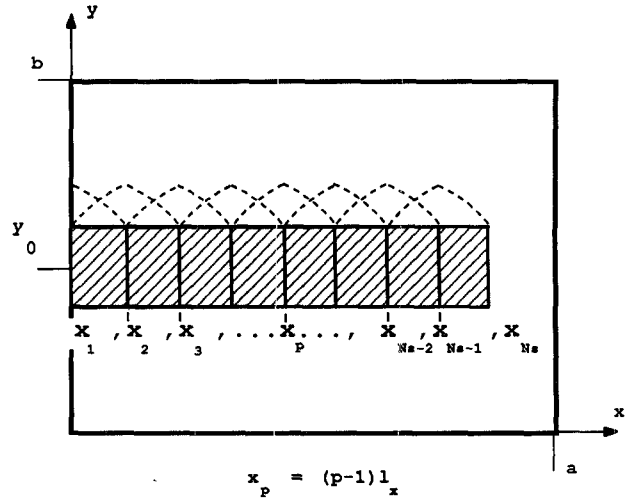

Fig. 3. Strip geometry for expansion of longitudinal current into overlapping sinusoidal basis functions.

A. Integral Equation

In the theoretical formulation, a few simplifying assumptions are made to reduce unnecessary complexity and excessive computer time. Throughout the analysis, it is assumed that the width of the conducting strips is small compared to the microstrip wavelength λ_g (the "thin-strip" approximation). In this case, the transverse component of the current may be neglected. While substrate losses are accounted for, it is assumed that the strip conductors and the walls of the shielding box are lossless and that the strip has infinitesimal thickness. These assumptions are valid for the high-frequency analysis of the microstrip structures of Fig. 2, provided good conductors are used in the metalized areas.

Consider the geometry of Fig. 1. In most cases the coaxial feed, or "launcher," is designed to allow only transverse electromagnetic (TEM) propagation, and the feed's center conductor is small compared to a wavelength ($kr_a \ll 1$). In these cases, the radial electric field will be dominant in the aperture and we can replace the feed by an equivalent magnetic surface current $\bar{M}_s$ [9]. This current is sometimes called a frill current. The source $\bar{M}_s$ induces the current distribution $\bar{J}_s$ on the conducting strip and produces the total electric field $\bar{E}^{\text{tot}}$ and the total magnetic field $\bar{H}^{\text{tot}}$ inside the cavity as indicated in Fig. 1.

Now consider a cavity geometry similar to Fig. 1, with the strip conductors as well as the coaxial input and output removed. Assume a test current $\bar{J}_q$ existing on a small subsection of the area which was occupied by the strip. The fields inside this new geometry are denoted by $\bar{E}_q$ and $\bar{H}_q$. Using the reciprocity theorem, the two sets of sources ($\bar{M}_s$, $\bar{J}_s$; and $\bar{J}_q$) are related according to

$$\int\int\int_V \left(\bar{J}_s \cdot \bar{E}_q - \bar{H}_q \cdot \bar{M}_s\right) dv = \int\int\int_V \bar{J}_q \cdot \bar{E}^{\text{tot}}\, dv \qquad (1)$$

where V represents the volume of the interior of the cavity.

Note that the reciprocity theorem has been widely used for developing integral equations similar to (1) for application to antenna and scattering problems [10]–[12]. Since $\bar{J}_q \cdot \bar{E}^{\text{tot}}$ is zero everywhere inside the cavity, the right-hand side of (1) vanishes. Reducing the remaining volume integrals in (1) to surface integrals results in

$$\int\int_{S_{\text{strip}}} \bar{E}_q(z=h) \cdot \bar{J}_s\, ds = \int\int_{S_f} \bar{H}_q(x=0) \cdot \bar{M}_s\, ds \qquad (2)$$

where S_{strip} is the surface of the conducting strip and S_f is the surface of the coaxial aperture(s). For one-port discontinuities, S_f represents the surface of the feed on the left-hand side of Fig. 1, while for two-port discontinuities S_f represents both feed surfaces. An integral equation similar to (2) can be derived for the case of gap generator excitation by setting $\bar{M}_s = 0$ and assuming that E_x is nonzero at one point on the strip [8].

In order to solve the integral equation (2), the current distribution $\bar{J}_s$ is expanded into a series of orthonormal functions as follows[1]:

$$\bar{J}_s = \psi(y) \sum_{p=1}^{N_s} I_p \alpha_p(x) \hat{x} \qquad (3)$$

where I_p are unknown current coefficients and N_s is the number of sections considered on the strip (Fig. 3). The function $\psi(y)$ describes the transverse variation of the current and is given by [2], [13]

$$\psi(y) = \begin{cases} \dfrac{\dfrac{2}{\pi W}}{\sqrt{1-\left[\dfrac{2(y-Y_0)}{W}\right]^2}}, & Y_0 - W/2 \leq y \leq Y_0 + W/2 \\ 0, & \text{otherwise} \end{cases} \qquad (4)$$

where W is the width of the microstrip line and Y_0 is the y coordinate of the center of the strip with respect to the origin in Fig. 1.

[1]The assumed time dependence is $e^{j\omega t}$.

The basis functions $\alpha_p(x)$ are described by

$$\alpha_p(x) = \begin{cases} \dfrac{\sin\left[K(x_{p+1}-x)\right]}{\sin(Kl_x)}, & x_p \leqslant x \leqslant x_{p+1} \\ \dfrac{\sin\left[K(x-x_{p-1})\right]}{\sin(Kl_x)}, & x_{p-1} \leqslant x \leqslant x_p \\ 0, & \text{otherwise} \end{cases} \tag{5}$$

for $p \neq 1$, and

$$\alpha_1(x) = \begin{cases} \dfrac{\sin\left[K(l_x-x)\right]}{\sin(Kl_x)}, & 0 \leqslant x \leqslant l_x \\ 0, & \text{otherwise} \end{cases} \tag{6}$$

for $p=1$, where K is a scaling factor, taken to be equal to the wave number in the dielectric, x_p is the x coordinate of the pth subsection ($=(p-1)l_x$), and l_x is the subsection length ($l_x = x_{p+1} - x_p$). For computation, all of the geometrical parameters are normalized with respect to the dielectric wavelength (λ_d); hence the normalized scaling factor is equal to 2π.

The integral equation (2) can now be transformed into a matrix equation by substituting the expansion of (3) for the current $\bar{J}_s$. The result may be put in the form

$$[\boldsymbol{Z}][\boldsymbol{I}] = [\boldsymbol{V}]. \tag{7}$$

In the above, $[\boldsymbol{Z}]$ is an $N_s \times N_s$ impedance matrix, $[\boldsymbol{I}]$ is a vector composed of the unknown current coefficients I_p, and $[\boldsymbol{V}]$ is the excitation vector. The individual elements of the impedance matrix are given by

$$Z_{qp} = \int\int_{S_p} \bar{E}_q(z=h)\cdot\hat{x}\psi(y)\alpha_p(x)\,ds \tag{8}$$

where S_p is the area of the two subsections on either side of the point x_p. The elements of the excitation vector are found according to

$$V_q = \int\int_{S_f} \bar{H}_q \cdot \bar{M}_s\,ds. \tag{9}$$

Once the elements of the impedance matrix and excitation vector have been computed, the current distribution is found by solving (7) as follows:

$$[\boldsymbol{I}] = [\boldsymbol{Z}]^{-1}[\boldsymbol{V}]. \tag{10}$$

B. Evaluation of Impedance Matrix Elements

Before evaluating the elements of the impedance matrix, the Green's function associated with the electric current $\bar{J}_q$ is derived. To do this the cavity is divided into two regions: region 1 consists of the volume contained within the substrate ($z < h$), while region 2 is the volume above the substrate surface ($z > h$).

The integral form of the electric field is given in terms of the Green's function by

$$\bar{E}_q^i = -j\omega\mu_0 \int\int\int_V \left[\left(\bar{\bar{I}} + \frac{1}{k_i^2}\bar{\nabla}\bar{\nabla}\right)\cdot\left(\bar{\bar{G}}^i\right)^T\right]\cdot\bar{J}\,dv' \tag{11}$$

where $k_i^2 = \omega^2\mu_0\epsilon_i$. The index i indicates that the above holds in each region (i.e., for $i=1,2$).

In (11), $\bar{\bar{G}}^i$ is a dyadic Green's function [14] satisfying the following equation:

$$\nabla^2\bar{\bar{G}}^i + k_i^2\bar{\bar{G}}^i = -\bar{\bar{I}}\delta(\bar{r}-\bar{r}') \tag{12}$$

where $\bar{\bar{I}}$ is the unit dyadic ($=\hat{x}\hat{x}+\hat{y}\hat{y}+\hat{z}\hat{z}$), $\bar{r}$ is the position vector of a field point anywhere inside the cavity, and $\bar{r}'$ is the position vector of an infinitesimal current source.

Because of the existence of an air–dielectric interface and the assumption of a unidirectional current, the dyadic Green's function will have the form

$$\bar{\bar{G}}^i = G_{xx}^i\hat{x}\hat{x} + G_{xz}^i\hat{x}\hat{z}. \tag{13}$$

The dyadic components of (13) are found by applying appropriate boundary conditions at the walls: $x=0, a$; $y=0, b$; and $z=0, c$; and at the air–dielectric interface [8]. These components may be expressed as

$$G_{xx}^{(1)} = \sum_{m=1}^{\infty}\sum_{n=0}^{\infty} A_{mn}^{(1)}\cos k_x x \sin k_y y \sin k_z^{(1)} z \tag{14}$$

$$G_{xz}^{(1)} = \sum_{m=1}^{\infty}\sum_{n=0}^{\infty} B_{mn}^{(1)}\sin k_x x \sin k_y y \cos k_z^{(1)} z \tag{15}$$

$$G_{xx}^{(2)} = \sum_{m=1}^{\infty}\sum_{n=0}^{\infty} A_{mn}^{(2)}\cos k_x x \sin k_y y \sin k_z^{(2)}(z-c) \tag{16}$$

$$G_{xz}^{(2)} = \sum_{m=1}^{\infty}\sum_{n=0}^{\infty} B_{mn}^{(2)}\sin k_x x \sin k_y y \cos k_z^{(2)}(z-c) \tag{17}$$

where

$$k_x = n\pi/a \tag{18}$$

$$k_y = m\pi/b \tag{19}$$

$$k_z^{(1)} = \sqrt{k_1^2 - k_x^2 - k_y^2} \tag{20}$$

$$k_z^{(2)} = \sqrt{k_0^2 - k_x^2 - k_y^2} \tag{21}$$

$$k_1 = \omega\sqrt{\mu_0\epsilon_1} \tag{22}$$

$$k_0 = \omega\sqrt{\mu_0\epsilon_0} \tag{23}$$

and

$$A_{mn}^{(1)} = \frac{-\varphi_n\cos k_x x' \sin k_y y' \tan k_z^{(2)}(h-c)}{abd_{1mn}\cos k_z^{(1)} h} \tag{24}$$

$$A_{mn}^{(2)} = \frac{-\varphi_n\cos k_x x' \sin k_y y' \tan k_z^{(1)} h}{abd_{1mn}\cos k_z^{(2)}(h-c)} \tag{25}$$

$$B_{mn}^{(1)} = \frac{-\varphi_n(1-\epsilon_r^*)k_x\cos k_x x' \sin k_y y' \tan k_z^{(1)} h \tan k_z^{(2)}(h-c)}{abd_{1mn}d_{2mn}\cos k_z^{(1)} h} \tag{26}$$

$$B_{mn}^{(2)} = \frac{-\varphi_n(1-\epsilon_r^*)k_x\cos k_x x' \sin k_y y' \tan k_z^{(1)} h \tan k_z^{(2)}(h-c)}{abd_{1mn}d_{2mn}\cos k_z^{(2)}(h-c)}. \tag{27}$$

In (24)–(27), ϵ_r^* is the complex dielectric constant of the substrate and

$$\varphi_n = \begin{cases} 2 & \text{for } n = 0 \\ 4 & \text{for } n \neq 0 \end{cases} \tag{28}$$

$$d_{1mn} = k_z^{(2)} \tan k_z^{(1)} h - k_z^{(1)} \tan k_z^{(2)} (h - c) \tag{29}$$

$$d_{2mn} = k_z^{(2)} \epsilon_r^* \tan k_z^{(2)} (h - c) - k_z^{(1)} \tan k_z^{(1)} h. \tag{30}$$

In view of (11)–(30), the elements of the impedance matrix may be put in the following form[2]:

$$Z_{qp} = \frac{j\omega\mu_0 K^2 l_x^4}{16ab \sin^2 Kl_x} \zeta_q \zeta_p \sum_{n=0}^{NSTOP} \varphi_n \cos k_x x_q \cos k_x x_p \cdot [\operatorname{sinc} R_{1n} \quad \operatorname{sinc} R_{2n}]^2 LN(n) \tag{31}$$

with $LN(n)$ given by the series

$$LN(n) = \sum_{m=1}^{MSTOP} L_{mn}. \tag{32}$$

The series elements L_{mn} are given by

$$L_{mn} = \frac{\varphi_n \left[\sin(k_y Y_0) J_0\left(\frac{k_y W}{2}\right) \right]^2 \tan k_z^{(1)} h \tan k_z^{(2)} (h - c)}{\left[k_z^{(2)} \tan k_z^{(1)} h - k_z^{(1)} \tan k_z^{(2)} (h - c) \right]} \cdot \frac{\left[k_z^{(2)} \epsilon_r^* \left(1 - \frac{k_x^2}{k_1^2}\right) \tan k_z^{(2)} (h - c) - k_z^{(1)} \left(1 - \frac{k_x^2}{k_0^2}\right) \tan k_z^{(1)} h \right]}{\left[k_z^{(2)} \epsilon_r^* \tan k_z^{(2)} (h - c) - k_z^{(1)} \tan k_z^{(1)} h \right]} \tag{33}$$

where Y_0 is the y coordinate of the center of the strip, and

$$\operatorname{sinc}(t) = \begin{cases} \dfrac{\sin t}{t} & \text{for } t \neq 0 \\ 1 & \text{for } t = 0 \end{cases} \tag{34}$$

$$\zeta_q = \begin{cases} 2 & \text{for } q = 1 \\ 4 & \text{otherwise} \end{cases} \tag{35}$$

$$R_{1n} = \frac{1}{2}(K + k_x) l_x \tag{36}$$

$$R_{2n} = \frac{1}{2}(K - k_x) l_x. \tag{37}$$

C. Evaluation of the Excitation Vector Elements

The formulation for the excitation vector elements for the one-port case will now be carried out. The case for two-port excitation is a straightforward extension [8].

To evaluate the excitation vector elements according to (9), we need to find the magnetic field $\bar{H}_q$ and the frill current $\bar{M}_s = M_\phi \hat{\phi}$. An approximate expression for the frill current is given by [9]

$$\bar{M}_s = -\frac{V_0}{\rho \ln\left(\frac{r_b}{r_a}\right)} \hat{\phi} \tag{38}$$

where V_0 is the complex voltage applied by the coaxial line at the feed point, r_b is the radius of the coaxial feed's outer conductor, r_a is the radius of the coaxial feed's inner conductor, and ρ, ϕ are cylindrical coordinates referenced to the feed's center.

Substituting from (38) into (9) yields (with $ds = \rho \, d\rho \, d\phi$)

$$\begin{aligned} V_q &= -\frac{V_0}{\ln\left(\frac{r_b}{r_a}\right)} \int\int_{S_f} H_{q\phi}^{i}(x = 0) \, d\rho \, d\phi \\ &= -\frac{V_0}{\ln\left(\frac{r_b}{r_a}\right)} \left[\int\int_{S_f^{(1)}} H_{q\phi}^{(1)}(x = 0) \, d\rho \, d\phi + \int\int_{S_f^{(2)}} H_{q\phi}^{(2)}(x = 0) \, d\rho \, d\phi \right] \end{aligned} \tag{39}$$

where $S_f^{(1)}$ is the portion of the feed surface below the substrate–air interface ($z'' = \rho \sin\phi \leqslant -t$); $S_f^{(2)}$ is the portion of the feed surface above the substrate ($z'' = \rho \sin\phi \geqslant -t$); and $H_{q\phi}^{(1)}(x = 0)$ and $H_{q\phi}^{(2)}(x = 0)$ are the $\hat{\phi}$ components of the magnetic field in regions 1 and 2, respectively, evaluated on the plane of the aperture.

After solving for the magnetic fields $H_{q\phi}^{i}(x = 0)$ and substituting the resulting expressions into (39), the following formulation is produced for excitation vector elements:

$$V_q = \frac{-V_0 \zeta_q K l_x^2}{\ln\left(\frac{r_b}{r_a}\right) 4ab \sin Kl_x} \sum_{n=0}^{NSTOP} \cos k_x x_q \cdot \operatorname{sinc} R_{1n} \quad \operatorname{sinc} R_{2n} \, [MN(n)] \tag{40}$$

where $MN(n)$ is expressed in terms of the series given by

$$MN(n) = \sum_{m=1}^{MSTOP} M_{mn}. \tag{41}$$

[2] The expression given here for the impedance matrix elements, and that given shortly for the excitation vector elements, apply to the case of an open-end or series gap. Slight modifications are necessary for analysis of parallel coupled line filters.

The series elements M_{mn} are given by the following integral:

$$M_{mn} = \int\int_{S_f} \mathcal{M}^{t}_{mn}\, d\rho\, d\phi$$

$$= \int\int_{S_f^{(1)}} \mathcal{M}^{(1)}_{mn}\, d\rho\, d\phi + \int\int_{S_f^{(2)}} \mathcal{M}^{(2)}_{mn}\, d\rho\, d\phi. \quad (42)$$

The above integrations are performed numerically, with the integrands $\mathcal{M}^{t}_{mn}$ given by

$$\mathcal{M}^{(1)}_{mn} = \cos\phi c^{(1)}_{zmn} \cos k_y(\rho\cos\phi + Y_c) \sin k_z^{(1)}(\rho\sin\phi + h_c)$$
$$- \sin\phi c^{(1)}_{ymn} \sin k_y(\rho\cos\phi + Y_c) \cos k_z^{(1)}(\rho\sin\phi + h_c) \quad (43)$$

for ρ and ϕ in region 1, and

$$\mathcal{M}^{(2)}_{mn} = \cos\phi c^{(2)}_{zmn} \cos k_y(\rho\cos\phi + Y_c)$$
$$\cdot \sin k_z^{(2)}(\rho\sin\phi - c + h_c) - \sin\phi c^{(2)}_{ymn} \sin k_y(\rho\cos\phi + Y_c)$$
$$\cdot \cos k_z^{(2)}(\rho\sin\phi - c + h_c) \quad (44)$$

for ρ and ϕ in region 2. In (43) and (44) Y_c and h_c are the y and z coordinates of the coaxial feed, and

$$c^{(1)}_{ymn} = \frac{c^{(1)}_{zmn}}{k_y d_{2mn}} \left\{ k_z^{(1)} k_z^{(2)} \epsilon_r^* \tan k_z^{(2)}(h-c) \right.$$
$$\left. - \left[\left(k_z^{(1)}\right)^2 + k_x^2(1-\epsilon_r^*) \right] \tan k_z^{(1)} h \right\} \quad (45)$$

$$c^{(1)}_{zmn} = \frac{\varphi_n k_y \tan k_z^{(2)}(h-c)}{d_{1mn} \cos k_z^{(1)} h} \sin k_y Y_0\, J_0\left(k_y \frac{W}{2}\right) \quad (46)$$

$$c^{(2)}_{ymn} = \frac{c^{(2)}_{zmn}}{k_y d_{2mn}} \left\{ k_z^{(1)} k_z^{(2)} \tan k_z^{(1)} h \right.$$
$$\left. - \left[\left(k_z^{(2)}\right)^2 \epsilon_r^* - k_x^2(1-\epsilon_r^*) \right] \tan k_z^{(2)}(h-c) \right\} \quad (47)$$

$$c^{(2)}_{zmn} = \frac{\varphi_n k_y \tan k_z^{(1)} h}{d_{1mn} \cos k_z^{(2)}(h-c)} \sin k_y Y_0\, J_0\left(k_y \frac{W}{2}\right). \quad (48)$$

The above outlines the theory for computing the current distribution on the conducting strips of shielded microstrip discontinuities. The next step is to use the current distribution to derive the network parameters of the discontinuity under consideration. However, since the methods used to derive network parameters are described elsewhere [2], [8], [15], only a brief summary is given in the Appendix.

The theoretical method developed above has been implemented in a Fortran program. The remainder of the paper addresses computational aspects of the solution for the current distribution and discontinuity network parameters.

III. Computation of Current Distribution

To gain insight into the nature of the computations, we will now examine plots of a typical impedance matrix, excitation vector, and current distribution for an open-ended microstrip line.

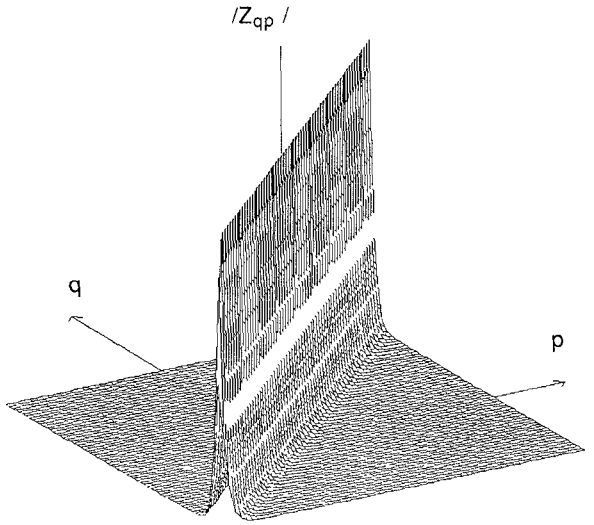

Fig. 4. Impedance matrix for an open end.

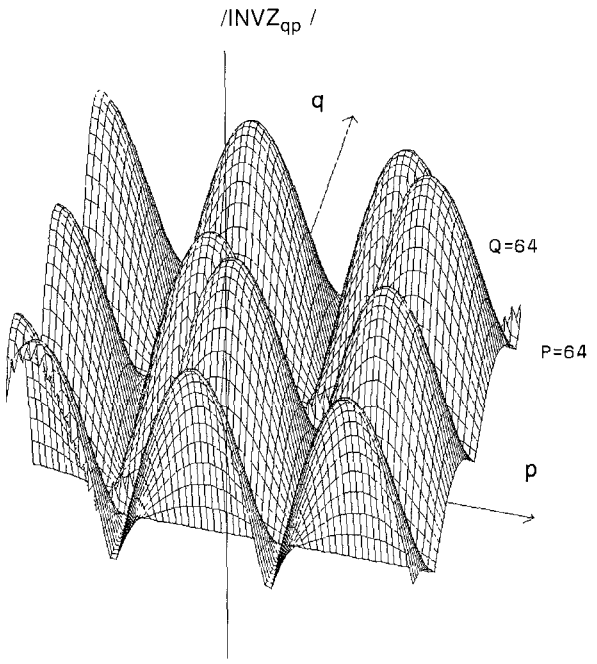

Fig. 5. Inverted impedance matrix for an open end. The sinusoidal shape of any row or column corresponds to the shape of the current distribution.

Fig. 4 shows the amplitude distribution of a typical impedance matrix. It is seen that the amplitude of the diagonal elements is the greatest and it tapers off uniformly as one moves away from the diagonal. Another observation is that the matrix is symmetric such that $Z_{qp} = Z_{pq}$ for any p and q, which is expected from (31). When the impedance matrix of Fig. 4 is inverted, the amplitude distribution is as shown in Fig. 5. The inverted impedance matrix shows a sinusoidal shape for any given row or column.

Fig. 6 shows the amplitude distribution for the excitation vector. The amplitude is highest over the subsection closest to the feed and then tapers off smoothly. In contrast, the excitation vector for the gap generator method has only one nonzero value, at the position of the source.

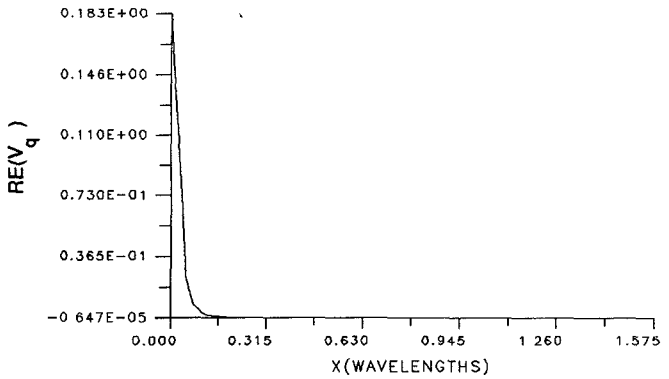

Fig. 6. Amplitude distribution of the excitation vector.

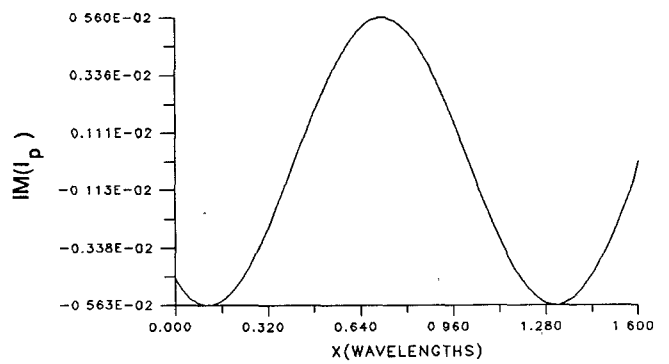

Fig. 7. Imaginary part of the current distribution for an open-ended line.

Multiplying the inverted impedance matrix by the excitation vector of Fig. 6 yields the current distribution of Fig. 7. It can be seen that the shape of the current is similar to that exhibited by the first column of the inverted impedance matrix. This is not surprising given the shape of the excitation vector.

IV. Convergence of Z_{qp} and V_q

In the expressions of (31) and (40) for the impedance matrix and excitation vector elements, the summations over m and n are theoretically infinite. The number of elements included in these series depends on the convergence behavior of Z_{qp} and V_q with the summation indices.

As seen from (31), the convergence of the impedance matrix is described mainly by the convergence of $LN(n)$. Fig. 8 shows the typical variation of $LN(n)$ with m and n. Most of the contributions from $LN(n)$ to the impedance matrix are concentrated in the first several n values. The convergence over m is good, and it appears that performing the computations out to $m = 200$ may be sufficient. Note, however, that the allowable truncation points for the summations over m and n vary with the geometry. The values quoted here are for illustration purposes only.

The computation of Z_{qp} over n is illustrated for a typical impedance matrix in Fig. 9. Shown is the convergence behavior for one row ($q = 32$) of the 64×64 element impedance matrix of Fig. 4. This behavior is representative of that for any row. After only a few terms the diagonal

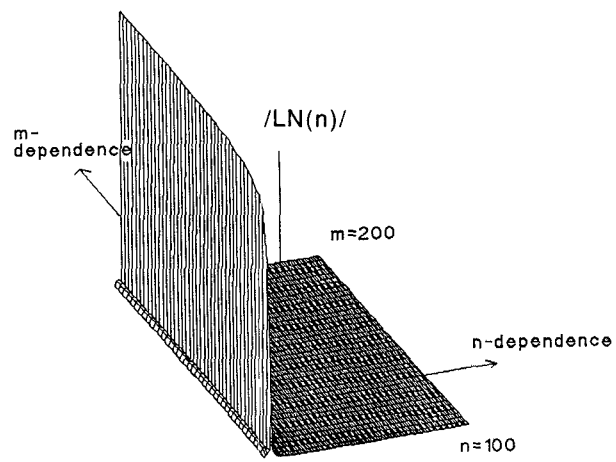

Fig. 8. Three dimensional plot of $LN(n)$ versus summation indices.

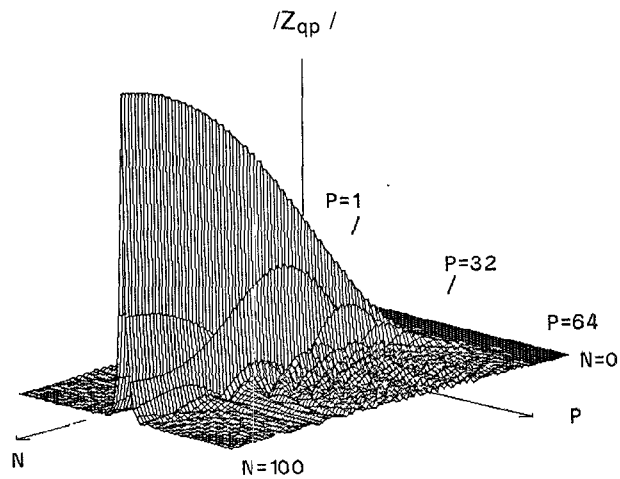

Fig. 9. Convergence of impedance matrix elements. A row ($q = 32$) of the matrix is seen to be well formed after adding 100 terms on n.

element ($p = q = 32$) rises above the others, and after adding 100 terms the amplitude distribution is well formed.

Similar conclusions can be drawn for the convergence of the excitation vector elements with respect to the summation indices m and n.

V. Convergence of Network Parameters

The convergence behavior of the elements of the impedance matrix and excitation vector is important to examine; yet the more relevant question remains: how are the final results affected by various convergence-related parameters?

To answer this question, a series of numerical experiments were carried out, and the main results are presented here. As illustrated in Fig. 10, an open-end discontinuity can be represented by either an effective length extension L_{eff} or an equivalent capacitance c_{op}. The microstrip effective dielectric constant ϵ_{eff} is calculated from the distance between two adjacent maxima of the open-end current distribution (Fig. 7).

The experiments investigated the convergence behavior of L_{eff} and ϵ_{eff} with respect to the sampling rate $N_x (= 1/l_x)$ and the truncation points $NSTOP$, $MSTOP$ for the

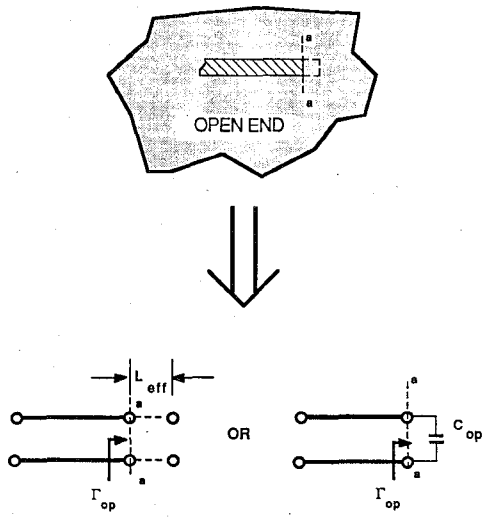

Fig. 10. Representation of a shielded microstrip open end.

summations over n and m, respectively. These numerical experiments have been grouped into three separate categories, each exploring a different aspect of the convergence behavior.[3]

A. *Effect of* K *Value*

Using the program mentioned above, data were generated to plot L_{eff} with ϵ_{eff} versus N_x for several different values of the normalized scaling factor K of (5) and (6). Fig. 11(a) shows the convergence behavior of L_{eff} for a typical case. It is seen that a relatively flat convergence region exists for all the K values between about 40 and 100 samples per wavelength. Outside this region the convergence behavior depends on K.

At first glance, it appears that the best convergence is achieved for higher K values (e.g. $K = 8\pi$); however, quite the opposite conclusion results from examining the ϵ_{eff} computation. As can be seen from Fig. 11(b), the best convergence for ϵ_{eff} is obtained for low K values.

Based on these and other observations [8], it was determined that a value of $K = 2\pi$ gives the best overall convergence behavior for the L_{eff} and ϵ_{eff} computations.

B. L_{eff}, ϵ_{eff} *Convergence on* n *and* m

To investigate the convergence of the network parameter computations with the summation index n, several program runs were executed for different values of $NSTOP$, with $MSTOP$ fixed at 1000. Data were generated to plot L_{eff} and ϵ_{eff} versus n for several l_x values. Fig. 12(a) shows that for all the l_x values, good convergence on n is achieved after 500 terms. The same can be said for the convergence of ϵ_{eff}.

In examining the convergence behavior with n it was found that, for a given subsection length l_x, cavity length a, and truncation point $NSTOP$, a maximum sampling limit exists beyond which the computed current becomes

[3]The parameters used for the plots shown in this section are as follows: $\epsilon_r = 9.7$, $W = h = 0.025$ in, $a = 3.5$ in, $b = c = 0.25$ in, $f = 18$ GHz.

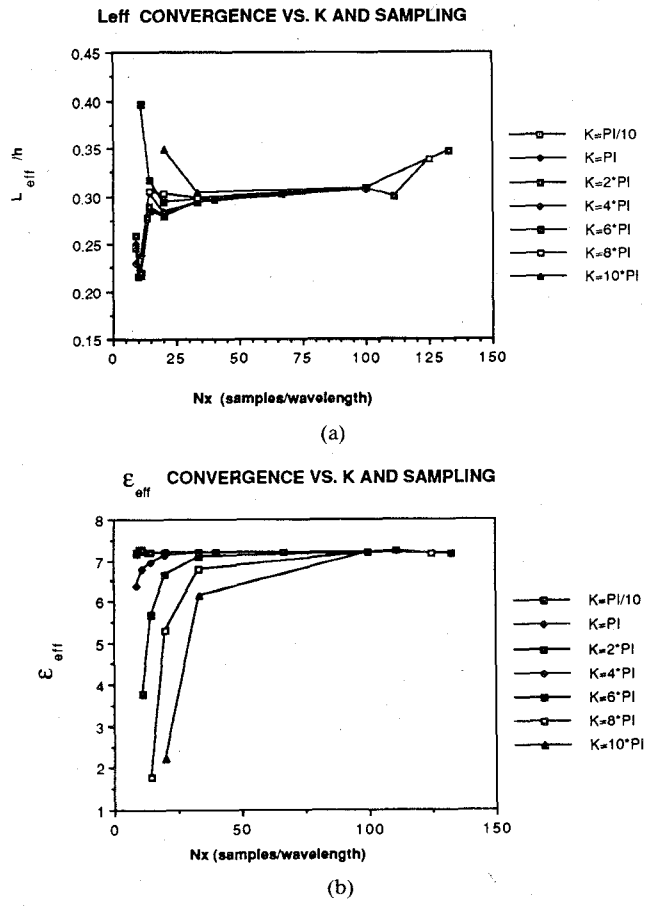

Fig. 11. Convergence of L_{eff} and ϵ_{eff} versus sampling.

completely erratic. This is called the erratic current condition and is given by the following simple relationship:

$$NSTOP * l_x < a \text{ or } N_x > \frac{NSTOP}{a}. \tag{49}$$

Outside of the region defined by (49), the numerical solution appears to be completely stable. To investigate the convergence behavior with respect to the summation index m, $NSTOP$ was fixed at 500, and the program was run for different values of $MSTOP$. Fig. 12(b) shows that L_{eff} converges well on m after about 500 terms. The convergence behavior of ϵ_{eff} on m was found to be similar to that for L_{eff}.

C. *Optimum Sampling Range*

In this last numerical experiment, the effect of varying l_x on the numerical accuracy of the matrix solution was examined. This was done by studying the variation of the matrix condition number [16] with respect to l_x for a fixed matrix size. After studying several cases it was found that an *optimum sampling range* may be defined by the following choice of subsection length l_x:

$$\frac{1.5a}{NSTOP} \leqslant l_x \leqslant \frac{4a}{NSTOP}. \tag{50}$$

Sampling within this range automatically avoids the erratic current condition and provides the best accuracy in the

matrix solution, and also in the solution for network parameters.

To support this last claim, consider the plot of Fig. 13. It is seen that the optimum sampling region specified by (50) coincides directly with the flat convergence region for the L_{eff} calculation. This consistency between the optimum sampling region and the flat convergence region for the L_{eff} calculation was observed in all the cases examined [8].

VI. Summary

In the theoretical part of the presented research, a method of moments formulation for the shielded microstrip problem was derived based on a more realistic excitation model than used with previous techniques. The formulation follows from the reciprocity theorem, with the use of a frill current model for the coaxial feed.

Computational considerations for implementing the theoretical solution were studied extensively. Several numerical experiments were presented that explored the convergence and the stability of the solution. Most significantly, it was found that an erratic current condition and an optimum sampling range exist; both of these are given by very simple relationships.

Appendix

A. One-Port Network Parameters (Open-End Discontinuity)

The effective length extension (Fig. 10) for an open-end discontinuity is given by

$$L_{\text{eff}} = \frac{\lambda_g}{4} - d_{\max} \tag{A1}$$

where $d_{\max}$ is the distance from the end of the line to a current maximum.

The normalized equivalent capacitance (Fig. 10) can be expressed as

$$c_{op} = \frac{\sin 2\beta_g d_{\max}}{\omega\left(1-\cos 2\beta_g d_{\max}\right)} = \frac{\sin 2\beta_g L_{\text{eff}}}{\omega\left(1+\cos 2\beta_g L_{\text{eff}}\right)}. \tag{A2}$$

In the above, β_g is the phase constant of microstrip transmission line.

B. Two-Port Network Parameters (Gap Discontinuity, Coupled Line Filters)

For the computation of two-port network parameters, the strip geometry is assumed to be physically symmetric with respect to the center of the cavity (in both the x and y directions of Fig. 1). The network parameters are determined by analyzing the current from the even- and odd-mode excitations as discussed in [2], [8], [15].

The normalized impedance parameters are given by

$$z_{11} = \frac{z^e_{\text{IN}} + z^o_{\text{IN}}}{2} \tag{A3}$$

$$z_{12} = \frac{z^o_{\text{IN}} - z^e_{\text{IN}}}{2} \tag{A4}$$

where z^e_{IN} and z^o_{IN} are the input impedances of the even- and odd-mode networks. The scattering parameters for the network may be derived using the following relations:

$$S_{11} = S_{22} = \frac{z_{11}^2 - 1 - z_{12}^2}{D} \tag{A5}$$

$$S_{12} = S_{21} = \frac{2z_{12}}{D} \tag{A6}$$

where

$$D = z_{11}^2 + 2z_{11} - z_{12}^2. \tag{A7}$$

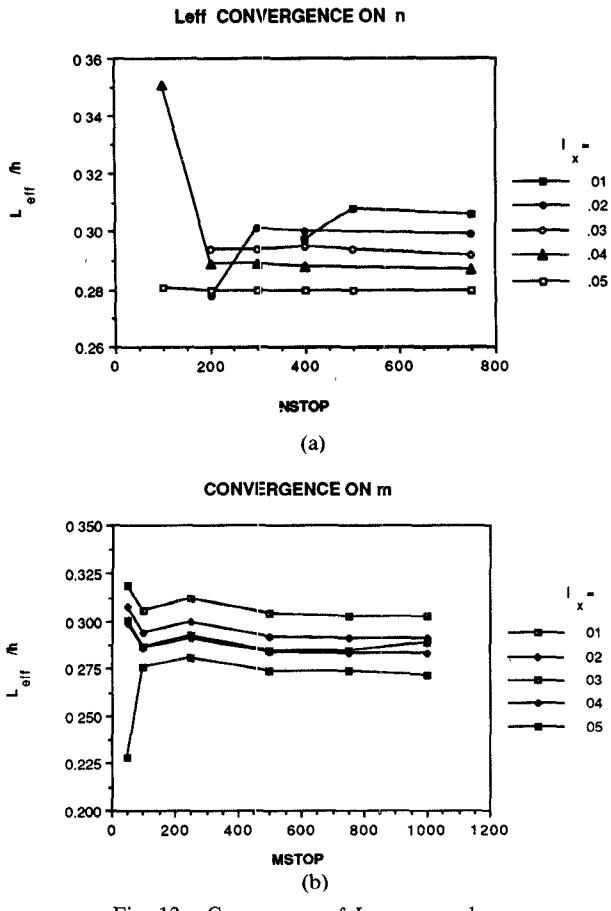

Fig. 12. Convergence of L_{eff} on n and m.

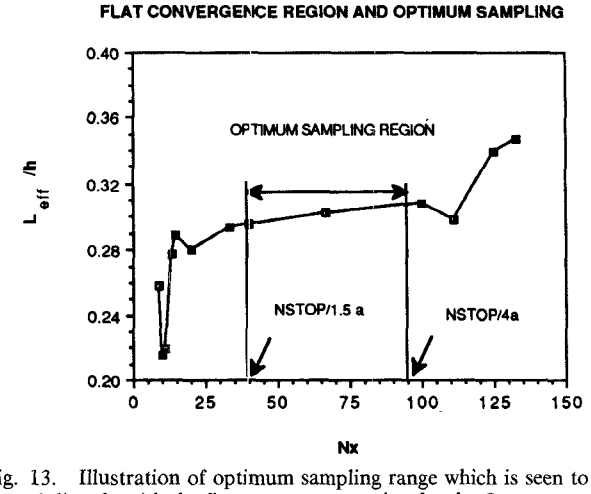

Fig. 13. Illustration of optimum sampling range which is seen to correspond directly with the flat convergence region for the L_{eff} computation.

ACKNOWLEDGMENT

The authors thank E. Watkins, J. Schellenberg, and M. Tutt for their contributions to this work.

REFERENCES

[1] R. H. Jansen and N. H. L. Koster, "Accurate results on the end effect of single and coupled lines for use in microwave circuit design," *Arch. Elek. Ubertragung.*, vol. 34, pp. 453–459, 1980.

[2] P. B. Katehi and N. G. Alexopoulos, "Frequency-dependent characteristics of microstrip discontinuities in millimeter-wave integrated circuits," *IEEE Trans. Microwave Theory Tech.*, vol. MTT-33, pp. 1029–1035, Oct. 1985.

[3] R. H. Jansen, and W. Wertgen, "Modular source-type 3D analysis of scattering parameters for general discontinuities, components and coupling effects in (M)MICs," in *Proc. 17th European Microwave Conf.* (Rome), 1987, pp. 427–432.

[4] J. C. Rautio, "An electromagnetic time-harmonic analysis of shielded microstrip circuits," *IEEE Trans. Microwave Theory Tech.*, vol. MTT-35, pp. 726–729, 1987.

[5] R. H. Jansen, "Hybrid mode analysis of end effects of planar microwave and millimeter-wave transmission lines," *Proc. Inst. Elec. Eng.*, vol. 128, pp. 77–86, Apr. 1981.

[6] T. Itoh, "Analysis of microstrip resonators," *IEEE Trans. Microwave Theory Tech.*, vol. MTT-22, pp. 946–951, 1974.

[7] L. P. Dunleavy and P. B. Katehi, "Shielding effects in microstrip discontinuities," pp. 1767–1774, this issue.

[8] L. P. Dunleavy, "Discontinuity characterization in shielded microstrip: A theoretical and experimental study," Ph.D. dissertation, University of Michigan, Apr. 1988.

[9] R. F. Harrington, *Time-Harmonic Electromagnetic Fields*. New York: McGraw-Hill, 1961, pp. 111–112.

[10] C. Chi and N. G. Alexopoulos, "Radiation by a probe through a substrate," *IEEE Trans. Antennas Propagat.*, vol. AP-34, pp. 1080–1091, Sept. 1986.

[11] N. N. Wang, J. H. Richmond, and M. C. Gilreath "Sinusoidal reaction formulation for radiation and scattering from conducting surfaces," *IEEE Trans. Antennas Propagat.*, vol. AP-23, pp. 376–382, May 1975.

[12] E. H. Newman and D. H. Pozar, "Electromagnetic modeling of composite wire and surface geometries," *IEEE Trans. Antennas Propagat.*, vol. AP-26, pp. 784–789, Nov. 1978.

[13] J. C. Maxwell, *A Treatise on Electricity and Magnetism*, 3rd. ed., vol. 1. New York: Dover, 1954, pp. 296–297.

[14] C. T. Tai, *Dyadic Green's Functions in Electromagnetic Theory*. Scranton, PA: Intext Educational Publishers, 1971.

[15] P. B. Katehi, "Radiation losses in mm-wave open microstrip filters," *Electromagnetics*, vol. 7, pp. 137–152, 1987.

[16] G. H. Golub and C. F. Van Loan, *Matrix Computations*. Baltimore, MD: John Hopkins University Press, 1983, pp. 26–27.

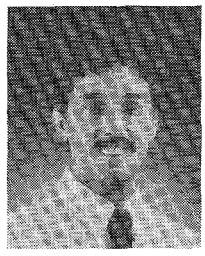

Lawrence P. Dunleavy was born in Detroit, MI, on September 16, 1959. He received the B.S.E.E. degree from Michigan Technological University, Houghton, in 1982 and the M.S.E.E. and Ph.D. degrees in electrical engineering from the University of Michigan, Ann Arbor, in 1984 and 1988, respectively. His Ph.D. research was in the area of numerical analysis and measurement of microstrip structures.

From 1982 to 1983 he worked at the ECI division of E-Systems Inc., St. Petersburg, FL, where he provided production support and design engineering for hybrid microwave circuitry. In 1983 he began graduate studies at the University of Michigan under a Schlumberger Graduate Fellowship. In 1984 he joined Hughes Aircraft Company as part of the Howard Hughes Doctoral Fellowship program. At the Space and Communication Group of Hughes, El Segundo, CA, he worked on system analysis of a millimeter-wave phased array antenna. In 1985 he transferred to the Industrial Electronics Group of Hughes, Torrance, CA, where his current responsibilities include research and development of new techniques for microwave and millimeter-wave measurements, and the design of GaAs-based hybrid and monolithic circuits operating in the 10–40 GHz frequency range.

Dr. Dunleavy is a member of the IEEE MTT and AP-S societies, Tau Beta Pi, Sigma Xi, Eta Kappa Nu, and the Automatic RF Techniques Group (ARFTG).

✠

Pisti B. Katehi (S'81–M'84) received the B.S.E.E. degree from the National Technical University of Athens, Greece, in 1977 and the M.S.E.E. and Ph.D. degrees from the University of California, Los Angeles, in 1981 and 1984 respectively.

In September 1984 she joined the faculty of the EECS Department of the University of Michigan, Ann Arbor, as an Assistant Professor. Since then, she has been involved in the modeling and computer-aided design of millimeter-wave and near-millimeter-wave monolithic circuits and antennas.

In 1984 Dr. Katehi received the W. P. King Award and in 1985 the S. A. Schelkunoff Award from the Antennas and Propagation Society. In 1987 she received an NSF Presidential Young Investigator Award and a Young Scientist Fellowship awarded from URSI. Dr. Katehi is a member of IEEE AP-S, MTT-S and Sigma Xi.